Multifunctional Nanoemulsion Platform for Imaging Guided Therapy Evaluated in Experimental Cancer

Anita Gianella,[†,‡] Peter A. Jarzyna,[†] Venkatesh Mani,[†] Sarayu Ramachandran,[†] Claudia Calcagno,[†] Jun Tang,[†] Benjamin Kann,[†] Wouter J. R. Dijk,[†] Victor L. Thijssen,[§] Arjan W. Griffioen,[§] Gert Storm,[⊥] Zahi A. Fayad,[†] and Willem J. M. Mulder[†,*]

[†]Translational and Molecular Imaging Institute, Department of Radiology, Mount Sinai School of Medicine, New York, New York 10029, United States, [‡]Cardiology Monzino Center, 20138 Milan, Italy, [§]Angiogenesis Laboratory, Department of Medical Oncology, VUMC Cancer Center, Amsterdam, The Netherlands, and [⊥]Utrecht Institute for Pharmacological Science, Utrecht, The Netherlands

ABSTRACT Nanoparticle applications in medicine have seen a tremendous growth in the past decade. In addition to their drug targeting application and their ability to improve bioavailability of drugs, nanoparticles can be designed to allow their detection with a variety of imaging methodologies. In the current study, we developed a multimodal nanoparticle platform to enable imaging guided therapy, which was evaluated in a colon cancer mouse model. This "theranostic" platform is based on oil-in-water nanoemulsions and carries iron oxide nanocrystals for MRI, the fluorescent dye Cy7 for NIRF imaging, and the hydrophobic glucocorticoid prednisolone acetate valerate (PAV) for therapeutic purposes. Angiogenesis-targeted nanoemulsions functionalized with $\alpha v\beta_3$-specific RGD peptides were evaluated, as well. When subcutaneous tumors were palpable, the nanoemulsions were administered at a dose of 30 mg of FeO/kg and 10 mg of PAV/kg. MRI and NIRF imaging showed significant nanoparticle accumulation in the tumors, while tumor growth profiles revealed a potent inhibitory effect in all of the PAV nanoemulsion-treated animals as compared to the ones treated with control nanoemulsions, the free drug, or saline. This study demonstrated that our nanoemulsions, when loaded with PAV, iron oxide nanocrystals, and Cy7, represent a flexible and unique theranostic nanoparticle platform that can be applied for imaging guided therapy of cancer.

KEYWORDS: nanoemulsions · theranostics · multimodal imaging · cancer nanotherapy · glucocorticoids

In the past decade, nanotechnology applications in medicine have seen a tremendous growth. This field, generally referred to as nanomedicine,[1] involves engineering of materials with nanoscale dimensions and multifunctional properties, such as nanoparticle probes that can be used for target-specific imaging.[2] An interesting feature of nanoprobes is their ability to be (simultaneously) detected using a variety of imaging methodologies, including magnetic resonance imaging (MRI),[3,4] near-infrared fluorescence (NIRF) imaging,[5] and nuclear imaging,[6] for both *in vitro* and *in vivo* studies.[7]

Even more advanced nanoprobes are the so-called "theranostic" multifunctional nanoparticles.[2,8] These nanoparticle platforms aim to diagnose disease and visualize nanoparticle accumulation and specifically and simultaneously deliver a drug, thereby facilitating the evaluation of treatment effects.[9] The aforementioned combination of targeted drug delivery and imaging of theranostic nanoparticles makes them especially attractive and promising for longitudinal evaluation of their therapeutic efficacy.

Trivially, but importantly, nanoparticle formulations offer a unique possibility to improve the pharmacokinetic profile of a drug.[10−12] Systemically administrated compounds are normally rapidly cleared from the circulation and accumulate in the target tissues at low concentrations.[13] In oncological practice, antitumor activity is generally obtained by applying high and frequent dosing of chemotherapeutic agents, which causes an array of adverse effects.[14,15] Moreover, water-insoluble compounds are difficult to administer and frequently require nonionic solubilizers to enable their intravenous administration.[16]

Interestingly, the mechanism of action of a drug may be very different when local accumulation is achieved at a diseased site using nanoparticulate formulations. For example, Banciu and colleagues demonstrated strong antitumor effects of long circulating liposomes that encapsulated glucocorticoids.[17,18] Commonly used as anti-inflammatory and immunosuppressive drugs, glucocorticoids can inhibit solid tumor growth in animals[19,20] at very high dose, but the pharmacological efficacy is associated with severe adverse effects. When water-soluble glucocorticoids are included

* Address correspondence to willem.mulder@mountsinai.org.

Received for review December 6, 2010 and accepted May 10, 2011.

Published online May 10, 2011
10.1021/nn103336a

A

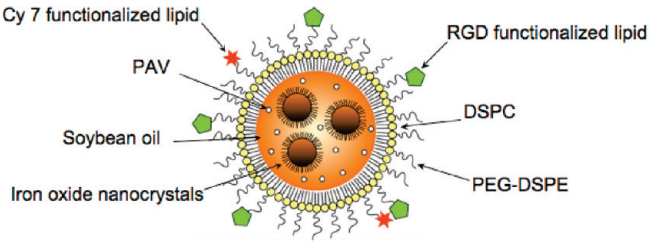

B

	Soy b.oil (mg)	PEG-DSPE (mmole)	DSPC (mmole)	Mal-PEG-DSPE (mmole)	PEG:DSPC:Mal (molar ratio)	PAV (mg)	FeO (mg)
CTRL nano	80	0.013	0.0138	-	0.94 : 1	-	-
PAV nano	80	0.013	0.0138	-	0.94 : 1	3.75	-
RGD-PAV nano	80	0.0115	0.0138	0.0014	0.83 : 1 : 0.1	3.75	-
FeO nano	80	0.013	0.0138	-	0.94 : 1	-	7.5
PAV+FeO nano	80	0.013	0.0138	-	0.94 : 1	3.75	7.5

C

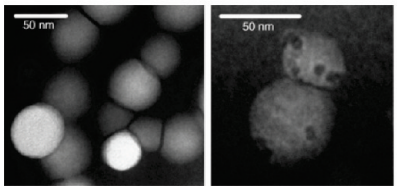

D

DLS size (nm) and Polydispersity				
PAV nano	RGD-PAV nano	PAV+FeO nano	FeO nano	CTRL nano
50.5 ± 0.14	48.4 ± 0.14	52.5 ± 0.13	50.7 ± 0.15	49.27 ± 0.14
0.137	0.138	0.128	0.150	0.143

Figure 1. Concept and nanoparticle characteristics. (A) Schematic of the nanoemulsion platform. (B) Overview of the composition of the different nanoemulsion formulations synthesized. (C) Negative staining transmission electron microscopy (TEM) of a typical nanoemulsion preparation without iron oxide nanocrystals (left) and with iron oxide nanocrystals (right). (D) Dynamic light scattering (DLS) size and polydispersity measurements.

in PEGylated liposomes, the adverse effects are strongly reduced and the local delivery to tumors is highly improved, which spectacularly enhances their efficacy.[21]

In the current study, a theranostic nanoparticle platform for multimodal imaging and the delivery of water-insoluble therapeutics was developed and evaluated in a colon cancer mouse model. It is based on a platform we developed recently[22] where an oil-in-water emulsion was formed from soybean oil, oleic acid coated iron oxide nanocrystals, and PEGylated lipids. The latter component is an amphiphilic molecule with a large hydrophilic fraction that facilitates the formation of relatively small nanoparticles. Oil-in-water microemulsions, composed of essentially similar (FDA) approved components, albeit with a much larger diameter, are routinely used as parenteral nutrition in patients.[23] The platform, schematically depicted in Figure 1A carries iron oxide nanocrystals for MRI, the fluorescent dye Cy7 for NIRF imaging, and the hydrophobic glucocorticoid prednisolone acetate valerate (PAV) for therapeutic purposes. In addition, angiogenesis-targeted nanoemulsions that were functionalized with $\alpha v\beta_3$-specific RGD peptides were evaluated, as well.

RESULTS AND DISCUSSION

We set out to develop a multimodal nanoparticle platform, based on oil-in-water nanoemulsions carrying iron oxide nanocrystals for MRI, as well as Cy5.5 or Cy7 fluorescent dye for NIRF imaging and the hydrophobic glucocorticoid prednisolone acetate valerate (PAV) for therapeutic purposes (Figure 1A). To synthesize the nanoemulsions, all of the components, such as soybean oil and lipids, were dissolved in chloroform. When appropriate, oleic acid coated iron oxide nanocrystals, rhodamine lipid, Cy5.5-DSPE or Cy7-PEG-DSPE lipid, and/or PAV were included, as well. The mixture was added dropwise to a 70 °C HEPES buffer under vigorous stirring to accomplish the immediate evaporation of chloroform and the formation of a crude oil-in-water emulsion. Subsequently, the formulations were homogenized and sized by sonication, washed with fresh HEPES buffer and concentrated using Vivaspin filter tubes.

In Figure 1B, the different nanoparticle formulations and their composition are shown. The morphology of the nanoparticles, with and without iron oxide nanocrystals, was investigated with TEM (Figure 1C). The hydrodynamic diameter of the different nanoemulsions was measured with dynamic light scattering (DLS). As shown in Figure 1D, the inclusion of additional functionalities and/or materials did not result in a change of diameter for the different nanoparticles (around 50 nm) or polydispersity. This relatively small size facilitates the extravasation of the nanoemulsions from the circulation over the tumor endothelium into the interstitial space, but also accommodates nanoparticle uptake by cells.

The drug inclusion in the final formulations was determined *via* spectrophotometric measurements. We determined the PAV inclusion efficiency, established for 11 different nanoemulsion formulations, to be 67.99 ± 9.18% of the initial input value.

The therapeutic effect of the different nanoemulsion formulations was investigated *in vitro* using a bioluminescent viability assay at a dose of 100 μg PAV/mL and a range of 270−380 μg Fe/mL. To study the acute and long-term effect on cell viability, two incubation schemes were applied: a 6 h incubation followed by washing and 18 h of cell growth, and a 24 h incubation. Macrophages, endothelial, and tumor cells were chosen because they represent important cellular components of a tumor.

The effects were expressed in % of viable cells compared to untreated control cells. After 6 h of exposure, LS174T tumor cells were the least affected (Figure 2A). A more pronounced effect at the same time point was observed for J774A1 macrophage cells (Figure 2C) that were incubated with PAV nanoemulsions, RGD-PAV nanoemulsions and PAV+FeO nanoemulsions and for HUVEC (Figure 2E) that were incubated with PAV nanoemulsions, RGD-PAV nanoemulsions, PAV+FeO nanoemulsions and FeO nanoemulsions. At 24 h, LS174T cells showed a significantly reduced viability after incubation with FeO and PAV+FeO nanoemulsions only (Figure 2B). Both J774A1 and HUVEC were very responsive to the treatment and displayed a very low viability after 24 h of incubations with FeO and PAV+FeO nanoemulsions. A loss of viability was also observed in J774A1 and HUVEC that were incubated with PAV nanoemulsions and RGD-PAV nanoemulsions (Figure 2D,F).

To visualize nanoemulsion uptake by the different cell types *in vitro*, MRI of cell pellets (Figure 2G,H) and fluorescence imaging of well plates were performed (Figure S1 in Supporting Information). We observed the different cell types avidly engulf the different nanoemulsion formulation, albeit at different levels depending on the cell type and nanoemulsion formulation used. Quenching effects, in both the MRI and the fluorescence imaging measurements, complicate the interpretation of the data and therefore cannot serve as a quantitative outcome.[24] To enable a fully quantitative evaluation of nanoemulsion uptake of the different formulations by the different cell types T_1 values (ms) were measured by Minispec benchtop NMR on HCl digested cell pellets. The relaxation rate R_1 ($1/T_1$, s^{-1}) directly correlates with the iron concentration. As expected, the highest R_1 values were found for J774A1 macrophages incubated with FeO and RGD-FeO nanoemulsions: 0.823 and 0.811 s^{-1}, respectively. The R_1 of HUVEC incubated with RGD-FeO nanoemulsions was 0.784 and 0.577 s^{-1} when incubated with FeO nanoemulsions, revealing the elevated uptake of RGD-functionalized nanoemulsions by endothelial cells, known to overexpress the $\alpha v\beta_3$ integrin.[25,26] For the LS174T tumor cells, also known to express $\alpha v\beta_3$ integrin,[27] we also observed different R_1 values, 0.618 and 0.695 s^{-1}, when incubated with FeO and RGD-FeO nanoemulsions, respectively. These data confirm that our nanoparticle platform functionalized with RGD peptides specifically interacts with $\alpha v\beta_3$ integrin expressing cell types.

In addition to the investigation of therapeutic response, which we will discuss in detail in the forthcoming sections, we performed MRI on the four mice selected (median sized tumors) from groups that were injected with CTRL nanoemulsions, PAV nanoemulsions, PAV+FeO nanoemulsions, and FeO nanoemulsions, using a 3T clinical scanner. Representative T_2*-weighted images of the aforementioned groups are presented in Figure 3. Tumors of animals injected with PAV nanoemulsions (Figure 3A) and CTRL nanoemulsions (Figure 3B) appeared bright compared to surrounding muscle tissue. On the other hand, the tumors of FeO+PAV and FeO nanoemulsion injected mice, shown in Figure 3C,D, respectively, appeared hypointense as compared to the tumors of mice injected with nanoemulsions that did not contain FeO, indicative of FeO accumulation in these tumors. We quantitatively evaluated the mean T_2* values of the tumors of the different groups. To that end, we generated T_2* maps from the T_2*-weighted images with different echo times (Figure S2 in Supporting Information). Figure 3E displays the T_2* map values and shows these in tumors of animals injected with nanoemulsions containing FeO to be 50% reduced compared to mice injected with nanoemulsions that did not contain FeO.

The inclusion of Cy7 NIR dye coupled lipid in the nanoemulsion corona enabled us to perform *in vivo* NIRF imaging to further corroborate the delivery and localization of the nanoparticles at the level of the entire animal. From preliminary *ex vivo* NIRF imaging data, we found the nanoparticles to accumulate in the liver, kidney, and tumors (Figure S3 in Supporting Information), with no significant differences between untargeted and RGD-targeted nanoemulsion injected mice.

In the full study, four mice injected with PAV nanoemulsions labeled with Cy7-PEG-DSPE in the lipid corona (Cy7-labeled nanoemulsion) were imaged 48 h after the injection and prior to sacrifice. Four mice injected with PAV nanoemulsions that did not contain the Cy7-PEG-DSPE lipid served as controls. Preferential nanoemulsion accumulation in tumors was appreciated (Figure 4A). The mean photon count tumor/skin ratios obtained for Cy7-labeled nanoemulsion injected mice was 11.29 ± 4.96, compared to 0.83 ± 0.013 for mice injected with unlabeled nanoemulsions (Figure 4B).

Confocal laser scanning microscopy was performed on tumor sections to visualize nanoemulsion localization in the tumor tissue as well as to investigate differences in distribution between the untargeted and the $\alpha v\beta_3$-specific RGD-functionalized nanoemulsions. We observed

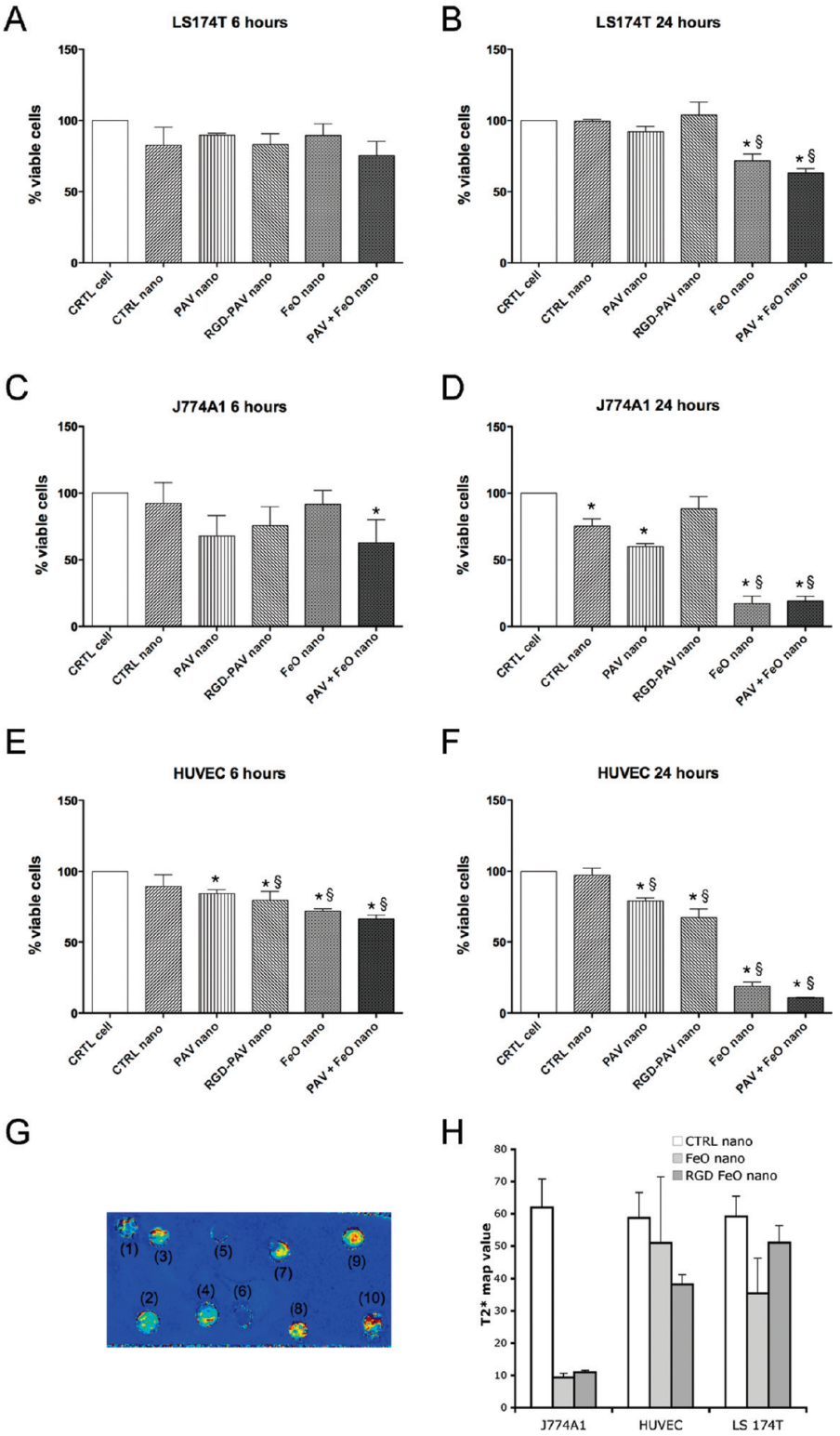

Figure 2. *In vitro* studies. (A,B) Viability of LS174T cancer cells after 6 and 24 h of incubation with the nanoemulsions (* *vs* CTRL cells $P < 0.001$, § *vs* CTRL-nano $P < 0.001$). (C) Viability of J774A1 macrophage cells after 6 h of incubation with the nanoemulsions (* *vs* CTRL cells $P < 0.05$) and (D) after 24 h of incubation with the nanoemulsions (* *vs* CTRL cells $P < 0.05$, § *vs* CTRL-nano $P < 0.001$). (E,F) Viability of endothelial cells (HUVEC) after 6 and 24 h of incubation with the nanoemulsions (* *vs* CTRL cells $P < 0.001$, § *vs* CTRL-nano $P < 0.001$). (G) T_2* map of cell pellets generated with a 3T scanner after 6 h of treatment with nanoemulsions. (1) HUVEC incubated with RGD-conjugated FeO nanoemulsions, (2) HUVEC incubated with FeO nanoemulsions, (3) LS174T incubated with RGD-conjugated FeO nanoemulsions, (4) LS174T incubated with FeO nanoemulsions, (5) J774A1 incubated with RGD-conjugated FeO nanoemulsions, (6) J774A1 incubated with FeO nanoemulsions, (7) HUVEC incubated with CTRL nanoemulsions, (8) LS174T incubated with CTRL nanoemulsions, (9) J774A1 incubated with CTRL nanoemulsions, (10) water as reference. (H) T_2* map values for the different cell pellets.

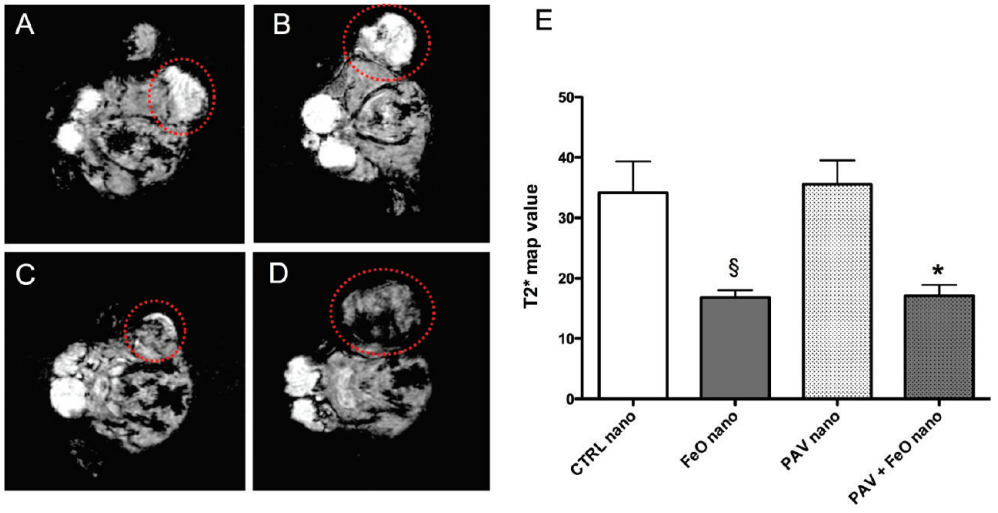

Figure 3. *In vivo* MRI at end of study. (A,B) Selected MR images of PAV nanoemulsion and CTRL nanoemulsion injected mice. (C,D) MR images of PAV+FeO nanoemulsion and FeO nanoemulsion injected mice. Red circles indicate the tumors. In (A) and (B), tumors appeared bright compared to surrounding muscle tissue. In (C) and (D), tumor areas appeared hypointense, indicative of FeO accumulation. (E) T_2* map mean values (ms) of the different groups (* *vs* PAV-nano $P < 0.05$, § *vs* CTRL-nano $P < 0.05$).

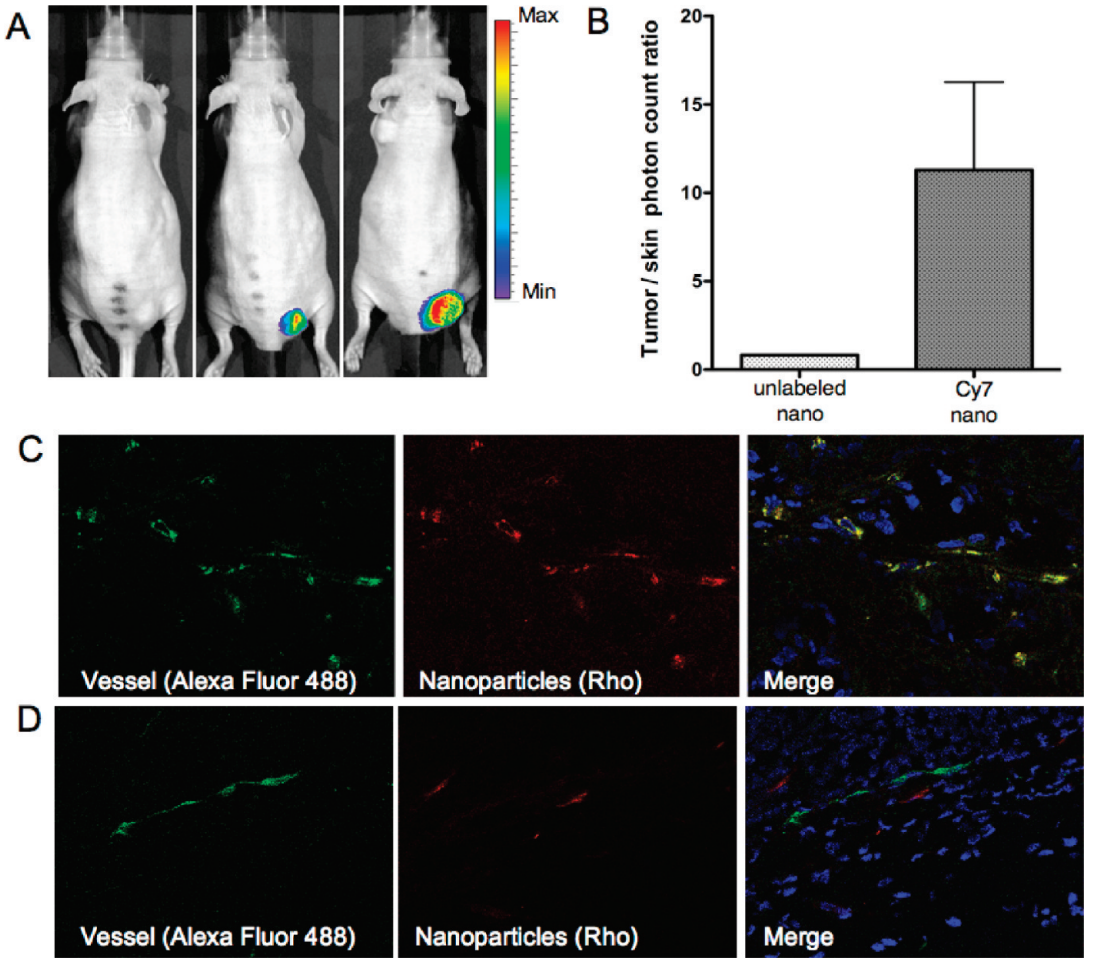

Figure 4. *In vivo* and *ex vivo* fluorescence imaging. (A) *In vivo* NIRF images of a mouse injected with unlabeled nanoemulsion (left) and mice (two different sized tumors) injected with Cy7 nanoemulsion (middle and right) at the end of the study. (B) Tumor/skin photon count ratio ($N = 4$) at the same time point. (C) Confocal images of blood vessels (isolectin, Alexa Fluor 488) and nanoparticles (Rhodamine B, red) of tumor tissue of mice injected with RGD-PAV nanoemulsions and (D) of mice injected with untargeted nanoemulsions.

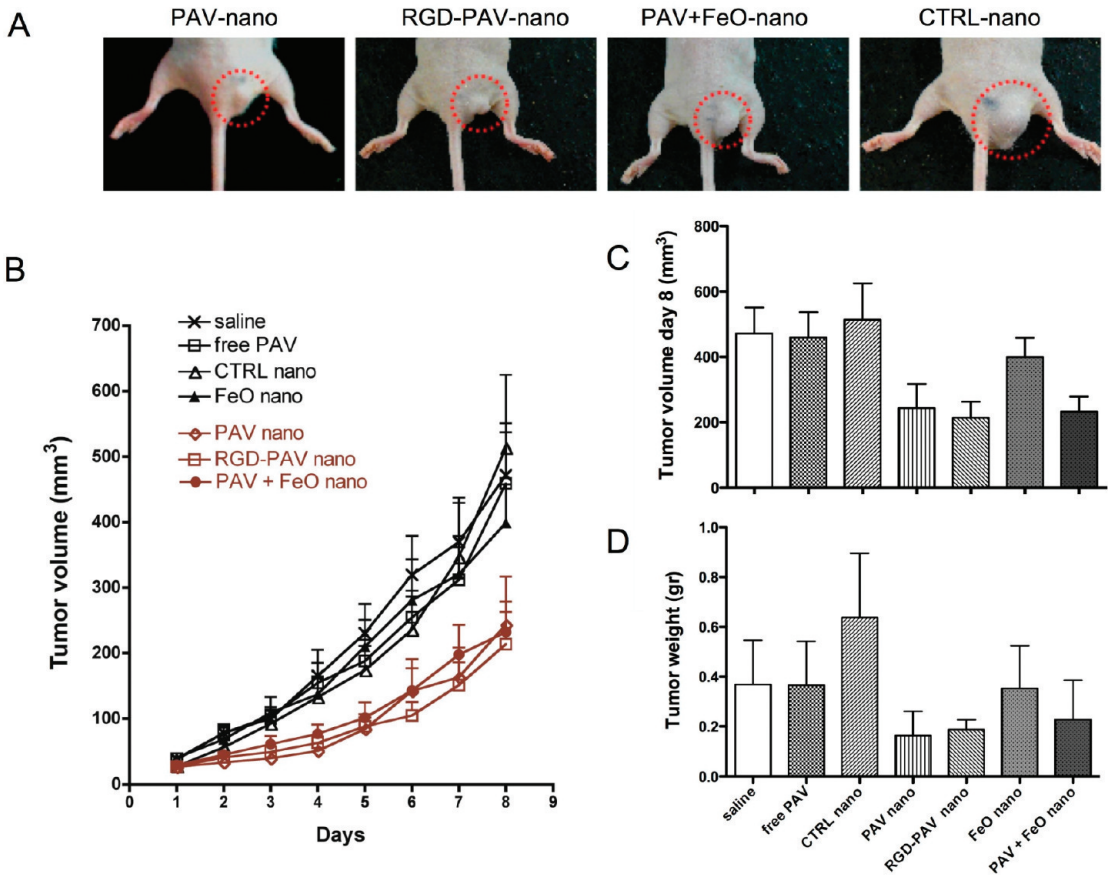

Figure 5. Therapeutic effect of nanoemulsions. (A) Photographs of typical tumors of mice injected with PAV nanoemulsion, RGD-PAV nanoemulsion, PAV+FeO nanoemulsion, and CTRL nanoemulsion. (B) Starting at day 6, tumor growth profiles showed statistically significant tumor growth inhibition ($P < 0.001$) in all of the PAV nanoemulsion treated groups compared to saline, CTRL nanoemulsions, FeO nanoemulsions, and free PAV injected groups. (C) Tumor volume measured by a caliper and (D) tumor weight at the end of the study.

the latter targeted nanoemulsions to be primarily colocalized with the vasculature (Figure 4C), while the untargeted nanoemulsions were found extravasated from the blood vessels in the tumor space (Figure 4D).

For the treatment studies, 56 mice (7 groups of 8 mice) were included. One group served as saline-treated control, one group was injected with free PAV, while the other 5 groups were treated with different nanoemulsion formulations. Treatment was initiated when tumors were palpable, and the tumor volumes were measured daily using a digital caliper throughout the treatment period. In Figure 5A, typical tumors at day 8 are displayed of mice treated with PAV nanoemulsions, RGD-PAV nanoemulsions, PAV+FeO nanoemulsions, and CTRL nanoemulsions. The tumor growth in mice injected with PAV nanoemulsions, RGD-PAV nanoemulsions, and PAV+FeO nanoemulsions was significantly inhibited compared to the mice injected with saline, CTRL nanoemulsions, FeO nanoemulsions, and free PAV at a dose of 10 mg PAV/kg (Figure 5B). At day 8, the mean tumor volume was 243.2 ± 73.5 mm^3 for PAV nanoemulsion treatment, 213.6 ± 49.2 mm^3 for RGD-PAV nanoemulsion treatment, and 232.1 ± 46.5 mm^3 for PAV+FeO nanoemulsion treatment (Figure 5C). At day 8, saline, free PAV, CTRL nanoemulsion, and FeO nanoemulsion treated animals displayed significantly larger tumor volumes of 471.7 ± 79.18, 459 ± 77.7, 513 ± 111.45, and 398.8 ± 59.13 mm^3, respectively (Figure 5C). To corroborate the tumor volumes measured by the digital caliper, we determined the tumor weight after the sacrifice (Figure 5D) and found a similar pattern. The correlation coefficient was established to be 0.779 (Figure S4 in Supporting Information). The data presented demonstrate that our nanoemulsions can be used as an effective drug delivery system for tumor therapy. As shown by the tumor growth profiles and tumor weight measurements, all of the PAV-loaded nanoemulsions induced a significant inhibition of the tumor growth compared to control groups. After three injections over a period of 8 days, the PAV-loaded nanoemulsion groups displayed tumor volumes that were at least 50% smaller than all control and free PAV groups at a dose of 10 mg/kg.

Prior to the above study, we conducted a pilot experiment where animals were also treated at a dose of 20 mg PAV/kg. This resulted in a 77% tumor growth inhibition (Figure S5 in Supporting Information) but

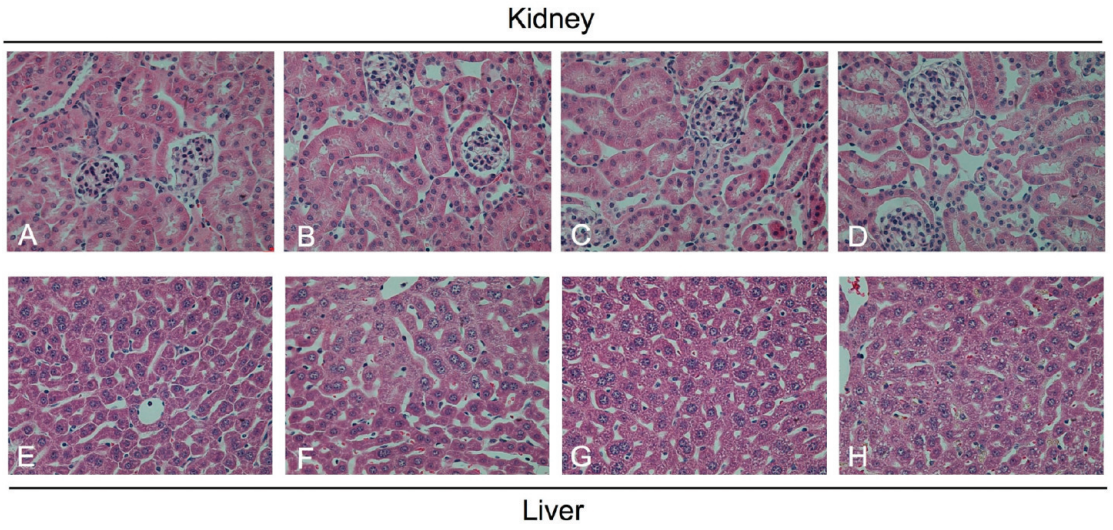

Figure 6. Histological analysis of kidney and liver tissues. (A−D) Kidney parenchyma, (E−H) liver parenchyma. (A,E) Tissue sections from saline injected mice, (B,F) tissue sections from free PAV injected mice, (C,G) tissue sections from PAV nanoemulsion injected mice, and (D,H) tissue section of PAV+FeO nanoemulsion injected mice. No relevant morphological changes were detected in these organs after any of the treatments.

was associated with severe weight loss, which motivated us to lower the dosing. At a dose of 10 mg/kg, we did not find any evidence of serious adverse effects, which is described in more detail below.

The effect of treatment on body weight was established by daily measurements. No relevant weight loss was observed for all groups, with a maximum, but nonsignificant, reduction of 11.55% in mice injected with PAV nanoemulsions at day 8 of treatment (Figure S6). After sacrifice, kidney and liver weights were recorded and normalized to body weights. When we compared the normalized data of the treated groups *versus* that of the saline groups, marginal variations were noticed in the kidney weights for all of the different groups and a marginal but not significant reduction of the liver weight/body weight ratio was observed in mice injected with CTRL nanoemulsions, PAV nanoemulsions, and RGD-PAV nanoemulsions (data not shown). In all of the groups treated with nanoemulsions and free PAV, kidney and liver histologic sections showed similar parenchyma morphology to the saline group, demonstrating that PAV and nanoemulsion administrations induced no toxic effects in these organs (Figure 6).

To clarify the therapeutic effect, both angiogenesis and inflammatory infiltration phenomena were studied. Despite the effects of some nanoemulsions on endothelial cell growth *in vitro*, staining and subsequent quantification of blood vessels in the tumors did not reveal significant changes between the different treatment modalities (Figure 7A,B). This was confirmed by analysis of mRNA expression of important growth factors and cell adhesion molecules involved in angiogenesis, which were not significantly altered following treatment (Figure S7A,B). To evaluate the infiltration of inflammatory cells into the tumors, immunostaining for CD68, a macrophage marker, was performed on tumor sections (Figure 7C). The area was measured and normalized to the total surface area of tumor sections analyzed. As shown in the graph in Figure 7D, the animals injected with saline, control nanoparticles, and FeO nanoparticles induced a lower macrophage infiltration compared to the mice injected with nanoparticle formulations containing PAV, although not all of the differences were statistically significant.

Most cancer chemotherapies are characterized by limited efficacy and strong side effects caused by the high and frequent dosing. Therefore, there is a strong motivation to develop treatment that enables efficient and safer drug delivery to tumors and, consequently, reduce dosages and collateral effects. Nanomedical treatments represent an attractive alternative and were pioneered over three decades ago with the introduction of liposomal drug formulations.[28] Currently, some of these formulations are applied in clinical practice,[29] but the success of liposomes is hampered by a variety of limitations, including the inability to include water-insoluble compounds, size them well below 100 nm, and relatively low encapsulation efficiencies. The past decade has seen unprecedented growth in the field of nanochemistry, which has resulted in the availability of numerous new nanomaterials to be potentially used for therapeutic and/or diagnostic purposes.

In a previous study, we developed and extensively characterized a new nanoparticle platform that was based on a small oil-in-water nanoemulsion,[22] which allows the delivery of hydrophobic agents and nanomaterials. In the present study, we modified this platform to obtain "theranostic" nanoemulsions to enable imaging guided treatment of experimental cancer. For diagnostic purposes, iron oxide nanocrystals were

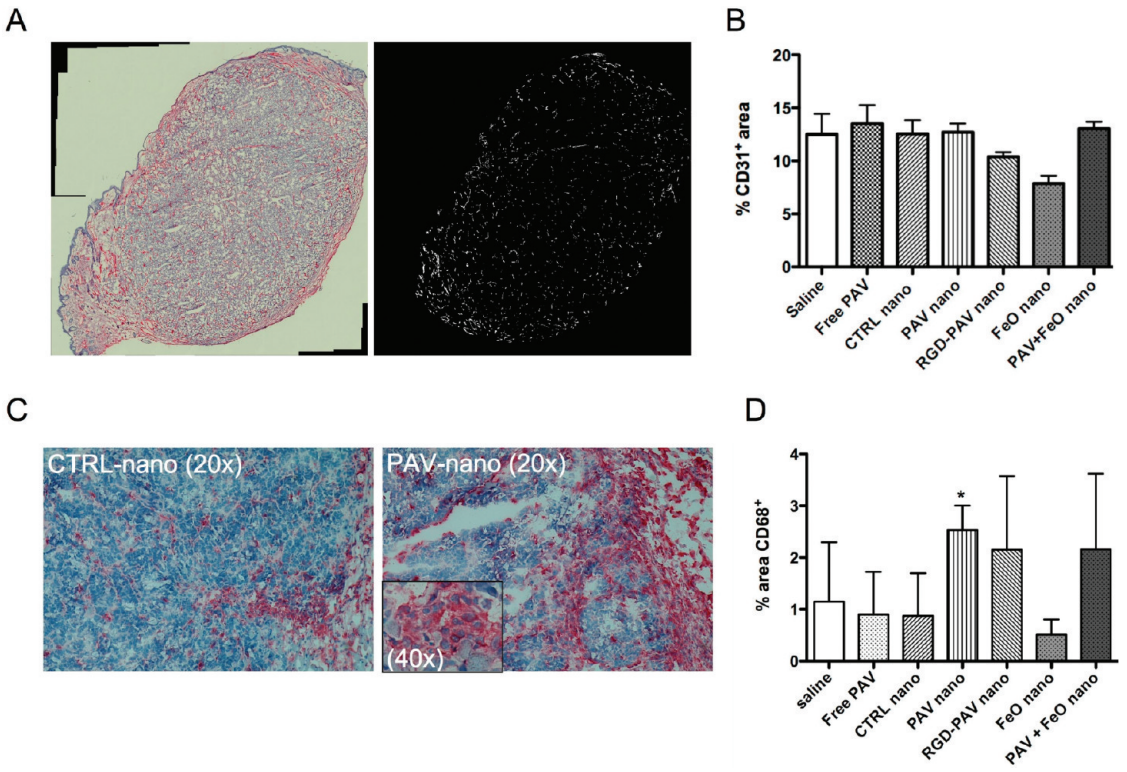

Figure 7. Angiogenesis and macrophage tumor infiltration evaluation. (A) Example of mosaic image (left) of tumor section stained for CD31, as well as threshold image of the same section used for CD31 quantification. Nonspecific signal of the skin was excluded. (B) CD31+ area of the entire tumor sections. (C) Macrophage infiltration in tumor section of mice injected with CTRL nanoemulsion and PAV nanoemulsion (magnification 20×). Inset shows the CD68+ cells at higher magnification (40×). (D) CD68+ mean area (* *vs* CTRL-nano $P < 0.05$).

included in the core and Cy7-conjugated lipid in the corona to enable *in vivo* MR and NIRF imaging, respectively. At day of sacrifice (day 8), dark areas were visible in tumors on T_2*-weighted MR images acquired in mice injected with FeO and PAV+FeO nanoemulsions. NIRF images acquired from mice injected with nanoemulsions containing Cy7-conjugated lipids revealed massive nanoemulsion accumulation in the tumors. We attribute the tumor accumulation of untargeted nanoemulsions to the enhanced permeability and retention effect, a phenomenon that occurs in tissues with a leaky vasculature, such as tumors and inflamed tissue.[30,31] On the other hand, RGD peptide-functionalized nanoemulsions accumulated in the tumor tissue by active targeting of tumor blood vessels as revealed by confocal microscopy. Moreover, for therapeutic purpose, we included a hydrophobic glucocorticoid (PAV) in the nanoemulsion formulation and tested the pharmacological effect in the same animals. We tested a number of glucocorticoids, but PAV was selected based on previous studies,[18] its hydrophobicity, and its high inclusion efficiency.

To study active targeting, the cyclic RGD pentapeptide was conjugated to malemide-functionalized PEG lipids that were included in the lipidic corona. This peptide is known to have a high affinity for $\alpha v\beta_3$ integrin,[32,33] which is overexpressed by angiogenically activated endothelium.[34] Vascular targeting is attractive because angiogenesis is required for tumor growth,[35] and the vasculature is readily accessible for targeting and does not require the nanoparticle to extravasate into the tumor interstitium. In a number of reports by us[36−38] and others,[39,40] this targeting strategy has been shown to be very valuable for target-specific imaging with a variety of nanoparticles, including liposomes, quantum dots, and microemulsions. In the present study, we observed that in mice treated with RGD-PAV nanoemulsions the tumor growth was inhibited. *Ex vivo* confocal imaging performed on tumor slices showed the nanoparticles colocalized with tumor blood vessels.

Expression of growth factors and receptors involved in angiogenesis measured at the mRNA level, as well as the CD31 positive area, did not show any significant difference between the groups. On the basis of our data, it seems that process of angiogenesis is not involved in the therapeutic effect. Another aspect that has been studied in relation to the antitumor mechanism is the macrophage tumor infiltration. Measuring the percentage of the tumor area with CD68-positive cells showed an interesting difference between mice injected with nanoemulsion containing PAV and the control groups. All of the groups treated with PAV-loaded nanoemulsions showed the same trend: a

higher infiltration of cell expressing CD68 compared to saline and control groups. It has been established before that tumor associated macrophages (TAMs) can have a double function. These TAMs can exert angiogenic effects by secreting cytokines such as IL-1, IL-8, and TNF-α[41−43] but can also release angiostatic factors such as IL-12, MMP-12, and IL-18.[44−46] Therefore, their presence is often associated with tumor progression, metastasis, and poor prognosis, but in some tumor types, including prostate[47] and stomach cancer,[48] the presence of TAMs appears to be associated with improved prognosis. Some studies[49,50] have shown that tumor endothelial cells have a suppressed expression of adhesion molecules reducing the leukocyte−vessel wall interactions. The present study suggests that the different nanoemulsions do not induce differences in macrophage infiltration by regulating the endothelial adhesion molecule makeup. While we did not see any differences in angiogenesis, our data suggest that in this particular tumor model the treatment induced an influx of TAMs that resulted in hampered tumor growth. Further studies are needed to unravel the exact mode of action.

CONCLUSION

We have developed and evaluated a 50 nm nanoemulsion platform that can carry hydrophobic materials and can be applied as a theranostic tool for simultaneous imaging guided drug delivery in cancer. The nanoemulsion components are biodegradable, and in the current study, we demonstrate efficient tumor growth inhibition with the inclusion of the hydrophobic glucocorticoid PAV. Interestingly, we observed that the inhibition was not related to angiogenesis but possibly involved enhanced macrophage infiltration. Future studies combining other water-insoluble anti-inflammatory, angiostatic, or cytostatic agents with different nanoemulsion formulations will further assess the applicability of theranostic nanoparticles for cancer treatment.

METHODS

Synthesis of the Nanoemulsions. For the nanoemulsion's synthesis, all of the lipophilic components were dissolved in chloroform. Stock solutions were prepared at the following concentrations: soybean oil at 100 mg/mL, DSPC and PEG-DSPE at 20 mg/mL, Mal-PEG-DSPE and PAV at 10 mg/mL, Cy5.5 DSPE and Cy7-PEG-DSPE 1 mg/mL, iron oxide nanocrystals at 25 mg/mL. The different components were mixed to yield chloroform solutions that contained 80 mg of soybean oil, 36.36 mg of PEG-DSPE, and 10.92 mg of DSPC (PEG-DSPE/DSPC molar ratio 0.94:1). To allow functionalization with RGD peptides, 4.24 mg of Mal-PEG-DSPE was added (PEG-DSPE/DSPC/Mal-PEG-DSPE molar ratio 0.83:1:0.1) at the expense of PEG-DSPE. Where appropriate, 3.75 mg of PAV, 7.5 mg of FeO, 80 μg of Rho-DSPE, 66.6 μg of Cy7, or 238 μg of Cy5.5 was included. In Figure 1B, an overview of the different formulations is depicted.

Nanoemulsions were synthesized as described previously.[22] In short, the above-mentioned chloroform mixtures were slowly dripped in 20 mL of HEPES buffer (2.38 g/L HEPES, 8 g/L NaCl) at 70 °C. Thereafter, the samples were homogenized by sonication for 15 min (level 20%, pulse 70%, devise: Biologics Inc., ultrasonic homogenizer model 150 V/T). Finally, the nanoemulsions were washed with HEPES buffer and concentrated using Vivaspin concentrators with a 100.000 MW cut off size. To obtain nanoemulsions functionalized with the RGD peptide, 160 μL of RGD stock solution (2.5 mg/mL) was activated with a deacetylation solution of pH 7 for 1 h. Subsequently, the activated peptide was added to the concentrated nanoemulsions and incubated overnight at 4 °C.

Dynamic Light Scattering and Transmission Electron Microscopy. The hydrodynamic size of the nanoemulsions was measured using a dynamic light scattering (DLS) device (Brookhaven Instrument Corporation). After the synthesis, 20 μL of each formulations was diluted in 2 mL of Millipore water. At least 4 nanoemulsions per group have been measured with 5 runs for measurement.

A Hitachi H7650 linked to SIA (Scientific Instrument and Applications) digital camera run by Maxim CCD software was used. Transmission electron microscopy (TEM) was performed on nanoemulsions diluted by a 1:10 or 1:20 ammonium acetate buffer and using 2% sodium phosphotungstate (pH = 7) negative staining as described by Forte and Nordhausen.[51]

Quantification of Drug Inclusion Efficiency. Spectrophotometry in the 200−600 nm range was applied to solutions of PAV and lipid components dissolved in chloroform and established the wavelength with the maximum difference between PAV and lipid absorbance to be 258 nm. Standard curves of PAV were acquired at this wavelength. Before and after concentrating the samples, precise volumes of each formulation were dried overnight. Subsequently, the samples were diluted in methanol/chloroform (1:9), and absorbances were measured at 258 nm. The final absorbance was calculated after correcting for the absorbance of nanoemulsions with same size and same amount of phospholipids that contained soybean oil, PEGylated lipids, and ordinary phospholipids only. The final drug concentration was calculated from the PAV standard curve and normalized volume.

Tumor Model and *In Vivo* Protocol. Six week old male Swiss nude mice (Taconic, Albany, NY) were given a standard rodent chow diet and water available *ad libitum*. All of the handling product materials were approved by the Mount Sinai School of Medicine Institutional Animal Care and Use Committee. To establish subcutaneous tumors, 2×10^6 LS174T cells were injected in the right flank. The tumor was induced in 56 mice that were randomized in 7 groups: mice treated with saline, free PAV, CTRL nanoemulsions, PAV nanoemulsions, RGD-PAV nanoemulsions, FeO nanoemulsions, and PAV+FeO nanoemulsions. When tumors were palpable (day 1), the treatment was started. Each mouse received at day 1, 3, and 6 a dose of nanoemulsions equivalent to 30 mg of FeO/kg and 10 mg of PAV/kg *via* tail vein injections. A dose corresponding to the same amount of lipids was injected in the group of mice treated with CTRL nanoemulsions. As a control, PAV solubilized in ethanol was injected at a dose 10 mg/kg as free drug. At day 8, selected mice were imaged by magnetic resonance imaging (MRI) and near-infrared fluorescence (NIRF) imaging prior to sacrifice. During the entire treatment period, the body weight and tumor volumes (mm^3) were measured daily with a digital caliper according to the formula $V = 0.52 \times a^2 \times b$, where a is the smallest and b the largest superficial diameter.

Prior to the full-blown study, we evaluated the therapeutic efficacy in a pilot study that included five animals per group. Two different doses of PAV (10 and 20 mg/kg) were evaluated.

***In Vivo* MR Imaging.** Forty-eight hours after the last tail vein injection, four mice per group with median tumor sizes from the groups administered with CTRL nanoemulsions, FeO nanoemulsions, PAV nanoemulsions, and PAV+FeO nanoemulsions were imaged at a 3T whole body MR scanner (Philips Achieva, X Series, Eindhoven, The Netherlands) using a custom built 30

mm mouse coil (Philips Medical Solutions, Hamburg, Germany). Scout images were acquired to locate the tumor, which was used to position a 3D multiecho GRE scan to generate T_2* maps. The field of view (FOV) was 30 × 30 × 18 mm^3, resulting in an in-plane resolution of 200 μm × 200 μm and 36 slices of 500 μm in thickness. The repetition time (T_R) was set at 150 ms; eight echoes were acquired with a minimum echo time (T_{E1}) of 2.7 ms and an echo spacing (ΔT_E) of 4.2 ms. A 15° flip angle and 1 signal average were chosen.

The T_2* maps were generated using in-house software routines written in Matlab. The T_2* map values were computed by fitting a monoexponential decay model to the signal intensities over all the T_E values at each pixel location. Linear least-squares fitting algorithms were used to fit the signal intensities to the model curve. The linear fitting model used a log−log transform to compute the fit, plotting the log of the signal intensities *versus* the T_E values. Subsequently, T_2* map values were computed as the inverse of the slope of this curve.

After the imaging experiments, mice were sacrificed under isofluorane anesthesia, perfused with PBS containing 20 U Heparin/mL, and the tumors excised and collected.

***In Vivo* Near-Infrared Fluorescence Imaging.** NIRF imaging experiments were performed using the IVIS-200 imaging system (Calipex, Xenogen, Alameda, CA). To allow the detection of the Cy7 dye, a 710−760 nm excitation filter and an 810−875 nm emission filter were used. Four mice injected with PAV nanoemulsion that did not contain Cy7-PEG-DSPE (unlabeled nanoemulsion) and four mice injected with PAV nanoemulsion that contained Cy7-PEG-DSPE in the lipid corona (Cy7 nanoemulsion) were imaged 48 h after the injection. Each mouse received 20 μg of Cy7 dye. A field of view of 12.2 cm × 12.2 cm and an excitation time of 4 s were chosen. The photon count was measured in the tumor and skin, and the ratio was calculated. After the imaging experiments, mice were sacrificed under isofluorane anesthesia, perfused with PBS/heparin, and the tumors were collected.

Confocal Laser Scanning Microscopy and Immunohistochemistry. At day 8, CTRL nanoemulsion injected mice (N = 4), PAV nanoemulsion injected mice (N = 4), and RGD-PAV nanoemulsion injected mice (N = 4) were iv injected with isolectin GS-IB4 Alexa Fluor 488 conjugated (Invitrogen Molecular Probes, Eugene, Oregon) 10 min before the sacrifice to label the vasculature. Subsequently, the mice were perfused with PBS and tumors collected in OCT for *ex vivo* fluorescence microscopy. Fresh cut tumor slices were stained with DAPI mounting media (Vector Laboratories, Burlingame CA) and immediately imaged with a Leica SP5-DM confocal microscope (Bannockburn, IL) to visualize the localization of the rhodamine signal (nanoemulsion particles) and the isolectin signal (endothelial cells).

For the histological analysis of macrophage infiltration and microvessel density, 5 μm sections were cut and fixed in acetone for 5 min at −20 °C. After the unspecific site blocking (4% rabbit serum in PBS for 10 min), sections were incubated with a rat anti-mouse CD68 primary antibody (AbD Serotec, Raleigh NC) and rat anti-mouse CD31 primary antibody (BD Pharmingen), respectively, diluted 1:250 and 1:100 in the presence of 4% rabbit serum. For the detection, a rabbit anti-rat secondary antibody and alkaline phosphatase method were used (Vector ABC kit, Vector Laboratories, Burlingame CA). Three to four tumors per group were stained for both of the markers. Digital pictures of entire tumor sections were acquired in bright field using Axioplan 2IE microscope (20× magnification), and digital mosaic was obtained using Axiovision 4.6.3 SP1 software. Adobe Photoshop CS and ImageJ programs were used to quantify the percentage of the area positive for CD68 and CD31.

Gene Expression Profiling. For RNA isolation, 10 × 10 μm thick cryosections were cut from the frozen tumor tissues. The sections were directly lysed in RLT buffer from the RNeasy kit (Qiagen, Venlo, The Netherlands), and total RNA was isolated following the suppliers instructions. On column DNase digestion was performed to remove any genomic DNA contaminations. Subsequently, RNA was eluted, and concentration and purity were assessed on a NanoDrop ND-1000 (NanoDrop Technologies, Wilmington, DE). cDNA synthesis was performed with the iScript cDNA synthesis kit (Bio-Rad, Veenendaal, The Netherlands) on 1 μg of total RNA according to the suppliers protocol. Following cDNA synthesis, nuclease-free water was added up to a final volume of 50 μL. Next, real-time PCR was performed on the CFX96 (BioRad) using the iQ SYBR Green PCR master mix (BioRad). Each PCR reaction was performed in a 25 μL volume containing 30 ng of cDNA, 12.5 μL of 2× iQ SYBR Green PCR master mix, and 1 μL of primer mix (10 μM forward primer, 10 μM reverse primer). The PCR profile was as follows: 10 min at 95 °C, followed by 40 cycles of 15 s at 95 °C and 30 s at 60 °C. Subsequently, a melting curve analysis was performed which consisted of 70 cycles of 10 s with a temperature increment of 0.5 °C/cycle starting at 60 °C. The obtained C_t value of each gene of interest was normalized to the C_t of the reference genes as follows: $C_{t,norm} = C_{t,goi} - C_{t,ref}$ with $C_{t,ref} = (C_{t,bACT} \times C_{t,CycloA} \times C_{t,b2MG}{}^{1/3}$, with norm = normalized, goi = gene of interest, and ref = reference gene.

Statistical Analysis. For statistial analysis of the *in vitro* cell viability experiments and T_2* map values, one-way ANOVA test was used. Two-way ANOVA was used to analyze the tumor growth profiles, and t test was applied to analyze immunohistochemistry data. The Mann−Whitney rank sum test was used to analyze gene expression data.

Acknowledgment. We would like to thank Rolando Nolasco for the histological cutting and staining. This work was financially supported by the Dutch Cancer Society UM2008-4101 and VU2009-4358 (V.L.T., A.W.G.). This work was also supported by the National Heart, Lung, and Blood Institute, National Institutes of Health, as a Program of Excellence in Nanotechnology (PEN) Award, Contract #HHSN268201000045C and by R01 EB009638 (Z.A.F.)

Supporting Information Available: Detailed material description, abbreviations, additional methods, and supporting figures are provided. This material is available free of charge *via* the Internet at http://pubs.acs.org.

REFERENCES AND NOTES

1. Cormode, D. P.; Skajaa, T.; Fayad, Z. A.; Mulder, W. J. M. Nanotechnology in Medical Imaging Probe Design and Applications. *Arterioscl., Thromb., Vasc. Biol.* **2009**, *29*, 992–1000.
2. Jarzyna, P. A.; Gianella, A.; Skajaa, T.; Knudsen, G.; Deddens, L. H.; Cormode, D. P.; Fayad, Z. A.; Mulder, W. J. M. Multifunctional Imaging Nanoprobes. *Wiley Interdiscip. Rev.: Nanomed. Nanobiotechnol.* **2010**, *2*, 138–150.
3. Strijkers, G. J.; Mulder, W. J.; van Tilborg, G. A.; Nicolay, K. MRI Contrast Agents: Current Status and Future Perspectives. *Anticancer Agents Med. Chem.* **2007**, *7*, 291–305.
4. Mulder, W. J.; Strijkers, G. J.; van Tilborg, G. A.; Griffioen, A. W.; Nicolay, K. Lipid-Based Nanoparticles for Contrast-Enhanced MRI and Molecular Imaging. *NMR Biomed.* **2006**, *19*, 142–164.
5. Medarova, Z.; Pham, W.; Farrar, C.; Petkova, V.; Moore, A. *In Vivo* Imaging of SiRNA Delivery and Silencing in Tumors. *Nat. Med.* **2007**, *13*, 372–377.
6. Mitra, A.; Nan, A.; Line, B. R.; Ghandehari, H. Nanocarriers for Nuclear Imaging and Radiotherapy of Cancer. *Curr. Pharm. Des.* **2006**, *12*, 4729–4749.
7. Pan, D.; Lanza, G. M.; Wickline, S. A.; Caruthers, S. D. Nanomedicine: Perspective and Promises with Ligand-Directed Molecular Imaging. *Eur. J. Radiol.* **2009**, *70*, 274–285.
8. Hartman, K. B.; Wilson, L. J.; Rosenblum, M. G. Detecting and Treating Cancer with Nanotechnology. *Mol. Diagn. Ther.* **2008**, *12*, 1–14.
9. Bhojani, M. S.; Van Dort, M.; Rehemtulla, A.; Ross, B. D. Targeted Imaging and Therapy of Brain Cancer Using Theranostic Nanoparticles. *Mol. Pharmaceutics* **2010**, *7*, 1921–1929.
10. Alexis, F.; Pridgen, E.; Molnar, L. K.; Farokhzad, O. C. Factors Affecting the Clearance and Biodistribution of Polymeric Nanoparticles. *Mol. Pharmaceutics* **2008**, *5*, 505–515.
11. Alexis, F.; Pridgen, E. M.; Langer, R.; Farokhzad, O. C. Nanoparticle Technologies for Cancer Therapy. *Handb. Exp. Pharmacol.* **2010**, 55–86.

12. Allen, T. M. Long-Circulating (Sterically Stabilized) Liposomes for Targeted Drug-Delivery. *Trends Pharmacol. Sci.* **1994**, *15*, 215–220.
13. Mozafari, M. R.; Pardakhty, A.; Azarmi, S.; Jazayeri, J. A.; Nokhodchi, A.; Omri, A. Role of Nanocarrier Systems in Cancer Nanotherapy. *J. Liposome Res.* **2009**, *19*, 310–321.
14. Brannon-Peppas, L.; Blanchette, J. O. Nanoparticle and Targeted Systems for Cancer Therapy. *Adv. Drug Delivery Rev.* **2004**, *56*, 1649–1659.
15. Ahmad, M. Z.; Akhter, S.; Jain, G. K.; Rahman, M.; Pathan, S. A.; Ahmad, F. J.; Khar, R. K. Metallic Nanoparticles: Technology Overview & Drug Delivery Applications in Oncology. *Expert Opin. Drug Delivery* **2010**, *7*, 927–942.
16. Gelderblom, H.; Verweij, J.; Nooter, K.; Sparreboom, A. Cremophor El: The Drawbacks and Advantages of Vehicle Selection for Drug Formulation. *Eur. J. Cancer* **2001**, *37*, 1590–1598.
17. Banciu, M.; Fens, M. H. A. M.; Storm, G.; Schiffelers, R. M. Antitumor Activity and Tumor Localization of Liposomal Glucocorticoids in B16 Melanoma-Bearing Mice. *J. Controlled Release* **2008**, *127*, 131–136.
18. Banciu, M.; Metselaar, J. M.; Schiffelers, R. M.; Storm, G. Liposomal Glucocorticoids as Tumor-Targeted Anti-Angiogenic Nanomedicine in B16 Melanoma-Bearing Mice. *J. Steroid Biochem. Mol. Biol.* **2008**, *111*, 101–110.
19. Wolff, J. E.; Guerin, C.; Laterra, J.; Bressler, J.; Indurti, R. R.; Brem, H.; Goldstein, G. W. Dexamethasone Reduces Vascular Density and Plasminogen Activator Activity in 9l Rat Brain Tumors. *Brain Res.* **1993**, *604*, 79–85.
20. Badruddoja, M. A.; Krouwer, H. G. J.; Rand, S. D.; Rebro, K. J.; Pathak, A. P.; Schmainda, K. M. Antiangiogenic Effects of Dexamethasone in 9l Gliosarcoma Assessed by MRI Cerebral Blood Volume Maps. *Neuro-Oncology* **2003**, *5*, 235–243.
21. Schiffelers, R. M.; Banciu, M.; Metselaar, J. M.; Storm, G. Therapeutic Application of Long-Circulating Liposomal Glucocorticoids in Auto-Immune Diseases and Cancer. *J. Liposome Res.* **2006**, *16*, 185–194.
22. Jarzyna, P. A.; Skajaa, T.; Gianella, A.; Cormode, D. P.; Samber, D. D.; Dickson, S. D.; Chen, W.; Griffioen, A. W.; Fayad, Z. A.; Mulder, W. J. M. Iron Oxide Core Oil-in-Water Emulsions as a Multifunctional Nanoparticle Platform for Tumor Targeting and Imaging. *Biomaterials* **2009**, *30*, 6947–6954.
23. Goulet, O.; Antebi, H.; Wolf, C.; Talbotec, C.; Alcindor, L. G.; Corriol, O.; Lamor, M.; Colomb-Jung, V. A New Intravenous Fat Emulsion Containing Soybean Oil, Medium-Chain Triglycerides, Olive Oil, and Fish Oil: A Single-Center, Double-Blind Randomized Study on Efficacy and Safety in Pediatric Patients Receiving Home Parenteral Nutrition. *J. Parenter. Enteral Nutr.* **2010**, *34*, 485–495.
24. Kok, M. B.; Hak, S.; Mulder, W. J. M.; van der Schaft, D. W. J.; Strijkers, G. J.; Nicolay, K. Cellular Compartmentalization of Internalized Paramagnetic Liposomes Strongly Influences Both T-1 and T-2 Relaxivity. *Magn. Reson. Med.* **2009**, *61*, 1022–1032.
25. Brooks, P. C.; Clark, R. A. F.; Cheresh, D. A. Requirement of Vascular Integrin $\alpha V\beta 3$ for Angiogenesis. *Science* **1994**, *264*, 569–571.
26. Mulder, W. J.; Strijkers, G. J.; Habets, J. W.; Bleeker, E. J.; van der Schaft, D. W.; Storm, G.; Koning, G. A.; Griffioen, A. W.; Nicolay, K. MR Molecular Imaging and Fluorescence Microscopy for Identification of Activated Tumor Endothelium Using a Bimodal Lipidic Nanoparticle. *FASEB J.* **2005**, *19*, 2008–2010.
27. McCarty, O. J.; Mousa, S. A.; Bray, P. F.; Konstantopoulos, K. Immobilized Platelets Support Human Colon Carcinoma Cell Tethering, Rolling, and Firm Adhesion under Dynamic Flow Conditions. *Blood* **2000**, *96*, 1789–1797.
28. Fendler, J. H.; Romero, A. Liposomes as Drug Carriers. *Life Sci.* **1977**, *20*, 1109–1120.
29. Anton, A.; Ruiz, A.; Segui, M. A.; Calvo, L.; Munoz, M.; Lao, J.; Sancho, F.; Fernandez, L. Phase I Clinical Trial of Liposomal-Encapsulated Doxorubicin Citrate and Docetaxel, Associated with Trastuzumab, as Neo-Adjuvant Treatment in Stages II and IIIa, Her2-Overexpressing Breast Cancer Patients. Geicam 2003-03 Study. *Ann. Oncol.* **2009**, *20*, 454–459.
30. Hashizume, H.; Baluk, P.; Morikawa, S.; McLean, J. W.; Thurston, G.; Roberge, S.; Jain, R. K.; McDonald, D. M. Openings between Defective Endothelial Cells Explain Tumor Vessel Leakiness. *Am. J. Pathol.* **2000**, *156*, 1363–1380.
31. Maeda, H.; Wu, J.; Sawa, T.; Matsumura, Y.; Hori, K. Tumor Vascular Permeability and the EPR Effect in Macromolecular Therapeutics: A Review. *J. Controlled Release* **2000**, *65*, 271–284.
32. Ruoslahti, E.; Pierschbacher, M. D. Arg-Gly-Asp: A Versatile Cell Recognition Signal. *Cell* **1986**, *44*, 517–518.
33. Kok, R. J.; Schraa, A. J.; Bos, E. J.; Moorlag, H. E.; Asgeirsdottir, S. A.; Everts, M.; Meijer, D. K. F.; Molema, G. Preparation and Functional Evaluation of Rgd-Modified Proteins as $\alpha V\beta 3$ Integrin Directed Therapeutics. *Bioconjugate Chem.* **2002**, *13*, 128–135.
34. Griffioen, A. W.; Molema, G. Angiogenesis: Potentials for Pharmacologic Intervention in the Treatment of Cancer, Cardiovascular Diseases, and Chronic Inflammation. *Pharmacol. Rev.* **2000**, *52*, 237–268.
35. Molema, G.; Griffioen, A. W. Rocking the Foundations of Solid Tumor Growth by Attacking the Tumor's Blood Supply. *Immunol. Today* **1998**, *19*, 392–394.
36. Chen, W.; Jarzyna, P. A.; van Tilborg, G. A. F.; Nguyen, V. A.; Cormode, D. P.; Klink, A.; Griffioen, A. W.; Randolph, G. J.; Fisher, E. A.; Mulder, W. J. M.; *et al.* Rgd Peptide Functionalized and Reconstituted High-Density Lipoprotein Nanoparticles as a Versatile and Multimodal Tumor Targeting Molecular Imaging Probe. *FASEB J.* **2010**, *24*, 1689–1699.
37. Mulder, W. J. M.; Castermans, K.; van Beijnum, J. R.; Egbrink, M. G. A. O.; Chin, P. T. K.; Fayad, Z. A.; Lowik, C. W. G. M.; Kaijzel, E. L.; Que, I.; Storm, G.; *et al.* Molecular Imaging of Tumor Angiogenesis Using $\alpha V\beta 3$-Integrin Targeted Multimodal Quantum Dots. *Angiogenesis* **2009**, *12*, 17–24.
38. van Tilborg, G. A. F.; Mulder, W. J. M.; van der Schaft, D. W. J.; Reutelingsperger, C. P. M.; Griffioen, A. W.; Strijkers, G. J.; Nicolay, K. Improved Magnetic Resonance Molecular Imaging of Tumor Angiogenesis by Avidin-Induced Clearance of Nonbound Bimodal Liposomes. *Neoplasia* **2008**, *10*, 1459–1469.
39. Liu, S. Radiolabeled Multimeric Cyclic Rgd Peptides as Integrin $\alpha V\beta 3$ Targeted Radiotracers for Tumor Imaging. *Mol. Pharmaceutics* **2006**, *3*, 472–487.
40. Sipkins, D. A.; Cheresh, D. A.; Kazemi, M. R.; Nevin, L. M.; Bednarski, M. D.; Li, K. C. P. Detection of Tumor Angiogenesis *In Vivo* by $\alpha V\beta 3$-Targeted Magnetic Resonance Imaging. *Nat. Med.* **1998**, *4*, 623–626.
41. Voronov, E.; Shouval, D. S.; Krelin, Y.; Cagnano, E.; Benharroch, D.; Iwakura, Y.; Dinarello, C. A.; Apte, R. N. Il-1 Is Required for Tumor Invasiveness and Angiogenesis. *Proc. Natl. Acad. Sci. U.S.A.* **2003**, *100*, 2645–2650.
42. Chen, J. J. W.; Yao, P. L.; Yuan, A.; Hong, T. M.; Shun, C. T.; Kuo, M. L.; Lee, Y. C.; Yang, P. C. Up-Regulation of Tumor Interleukin-8 Expression by Infiltrating Macrophages: Its Correlation with Tumor Angiogenesis and Patient Survival in Non-Small Cell Lung Cancer. *Clin. Cancer Res.* **2003**, *9*, 729–737.
43. Leek, R. D.; Harris, A. L. Tumor-Associated Macrophages in Breast Cancer. *J. Mammary Gland Biol. Neoplasia* **2002**, *7*, 177–189.
44. Coughlin, C. M.; Salhany, K. E.; Wysocka, M.; Aruga, E.; Kurzawa, H.; Chang, A. E.; Hunter, C. A.; Fox, J. C.; Trinchieri, G.; Lee, W. M. F. Interleukin-12 and Interleukin-18 Synergistically Induce Murine Tumor Regression Which Involves Inhibition of Angiogenesis. *J. Clin. Invest.* **1998**, *101*, 1441–1452.
45. Cornelius, L. A.; Nehring, L. C.; Harding, E.; Bolanowski, M.; Welgus, H. G.; Kobayashi, D. K.; Pierce, R. A.; Steven, D.; Shapiro, S. D. Matrix Metalloproteinases Generate Angiostatin: Effects on Neovascularization. *J. Immunol.* **1998**, *161*, 6845–6852.
46. Dirkx, A. E. M.; Egbrink, M. G. A. O.; Wagstaff, J.; Griffioen, A. W. Monocyte/Macrophage Infiltration in Tumors:

Modulators of Angiogenesis. *J. Leukocyte Biol.* **2006**, *80*, 1183–1196.
47. Shimura, S.; Yang, G.; Ebara, S.; Wheeler, T. M.; Frolov, A.; Thompson, T. C. Reduced Infiltration of Tumor-Associated Macrophages in Human Prostate Cancer: Association with Cancer Progression. *Cancer Res.* **2000**, *60*, 5857–5861.
48. Migita, T.; Sato, E.; Saito, K.; Mizoi, T.; Shiiba, K.; Matsuno, S.; Nagura, H.; Ohtani, H. Differing Expression of Mmps-1 and -9 and Urokinase Receptor between Diffuse- and Intestinal-Type Gastric Carcinoma. *Int. J. Cancer* **1999**, *84*, 74–79.
49. Melder, R. J.; Koenig, G. C.; Witwer, B. P.; Safabakhsh, N.; Munn, L. L.; Jain, R. K. During Angiogenesis, Vascular Endothelial Growth Factor and Basic Fibroblast Growth Factor Regulate Natural Killer Cell Adhesion to Tumor Endothelium. *Nat. Med.* **1996**, *2*, 992–997.
50. Griffioen, A. W.; Damen, C. A.; Blijham, G. H.; Groenewegen, G. Tumor Angiogenesis Is Accompanied by a Decreased Inflammatory Response of Tumor-Associated Endothelium. *Blood* **1996**, *88*, 667–673.
51. Forte, T. M.; Nordhausen, R. W. Electron Microscopy of Negatively Stained Lipoproteins. *Methods Enzymol.* **1986**, *128*, 442–457.